Advances in
Geo-Energy Research

Vol. 20, No. 3, p. 227-242, 2026

Original article

Multi-scale characterization of the influence mechanism of coal porous media structure on coal seam water injection

Yanpeng Cao[1], Hongwei Zhou[1,2]*, Zelin Liu[3], Senlin Xie[4], Xiaotong Sun[5,6], Wei Wu[7]

[1] *School of Energy and Mining Engineering, China University of Mining and Technology, Beijing 100083, P. R. China*
[2] *State Key Laboratory for Fine Exploration and Intelligent Development of Coal Resources, China University of Mining & Technology, Beijing 100083, P. R. China*
[3] *State Key Laboratory for Tunnel Engineering, China University of Mining and Technology, Beijing 100083, P. R. China*
[4] *College of Energy and Mining Engineering, Xi'an University of Science and Technology, Xi'an 710054, P. R. China*
[5] *Jinan Heavy Industry Co., Ltd., Jinan 250109, P. R. China*
[6] *School of Qilu Transportation, Shandong University, Jinan 250002, P. R. China*
[7] *Institute of Geotechnical Engineering, Boku University, Vienna 1180, Austria*

Keywords:
Coal seam water injection
relaxation rate
pore structure characterization
borehole
water loss

Cited as:
Cao, Y., Zhou, H., Liu, Z., Xie, S., Sun, X., Wu, W. Multi-scale characterization of the influence mechanism of coal porous media structure on coal seam water injection. Advances in Geo-Energy Research, 2026, 20(3): 227-242.
https://doi.org/10.46690/ager.2026.06.05

Abstract:
With increasing depths in coal mining, water injection into coal seams has become a crucial technology to enhance coalbed methane recovery, suppress dust, and prevent gas outbursts under high stress and geothermal conditions. Given this background, this study aims to elucidate the dynamic behavior of water injection, migration and evaporation in coal. To investigate pore-fracture connectivity and moisture transport mechanisms, coal samples drilled and collected from a coal mine in Inner Mongolia, China, were analyzed using a combination of multi-scale characterization techniques, enabling the characterization of the relationship between pore structure connectivity and water transport behavior. Nuclear magnetic resonance, computer tomography, and mercury intrusion porosimetry were jointly utilized to explore the pore structure at different scales, and nuclear magnetic resonance was further used for real-time online water injection monitoring, allowing the dynamic observation of water migration and distribution within the samples. The results indicate that borehole drilling significantly enhances permeability and connected porosity, controlling both injection rate and maximum water uptake. Moreover, water transport is governed by pore structure at different scales, with fine pores influencing adsorption and larger pores facilitating flow. Evaporation under elevated temperatures proceeds from rapid free-water loss to slower bound-water desorption, with borehole presence having a minimal effect. These findings provide key insights into the multi-scale control of water dynamics and offer a theoretical and experimental basis for optimizing coalbed water injection strategies in deep, high-temperature environments.

1. Introduction

With the ongoing economic development, energy demand has been on the rise and coal exploitation has advanced to increasingly greater depths (Aydin, 2014; Fairhurst, 2017; Tu et al., 2021). Fluidized mining has been proposed to exploit deep-seated coal seams (Xie et al., 2017), which are characterized by high geostress, elevated geothermal gradients and high pore pressures, thereby increasing the risk of severe production hazards (Liu et al., 2024; Wei et al., 2024; Lu

---

*Corresponding author.
E-mail address: cypcumtb@163.com (Y. Cao); zhw@cumtb.edu.cn (H. Zhou); liuzelin@cumtb.edu.cn (Z. Liu); xslcomeon@163.com (S. Xie); qq1538799313@163.com (X. Sun); wei.wu@boku.ac.at (W. Wu).

Yandy Scientific Press

Received April 19, 2026; revised May 15, 2026; accepted May 28, 2026; available online June 1, 2026.

Table 1. Results of the proximate analysis.

Moisture on air-dried basis (%)	Ash content on dry basis (%)	Volatile matter on dry basis (%)	Fixed carbon on dry basis (%)	Coke residue characteristics (-)
4.83	4.18	30.68	65.14	2

et al., 2025). Coalbed water injection is a key technology for deep resource development, playing important roles in cooling the working face, suppressing dust, and promoting coalbed methane recovery while mitigating gas outbursts (Xu et al., 2023; Wang et al., 2025). Water injection via boreholes alters the physico-mechanical properties of coal and its internal fluid-transport environment. In fact, the pore-fracture structure (PFS) is the primary control interface for water migration and distribution (Xie et al., 2015; Xu et al., 2026). To this end, the introduction of engineered boreholes further modifies the seepage field by coupling borehole conduits with the natural fracture network, significantly affecting the injection efficiency and extent. Meanwhile, as mining depth increases, high-temperature conditions exacerbate the evaporation and loss of injected water, directly limiting the engineering effectiveness of injection (Pei et al., 2024; Shen et al., 2025). Therefore, systematically revealing the full process of injection, migration and evaporation of water in coal under deep, high-temperature conditions is essential for optimizing deep coalbed water-injection techniques.

Regarding the field of coal water-injection research, considerable progress has been made in recent years. For instance, Wang et al. (2022) injected water into grooves around coal pillars to increase confinement and axial stress. By pressurizing cylinders with nitrogen and introducing surfactant solutions into pillar fractures, they studied the effects of the cationic surfactant (dodecyl-trimethylammonium bromide) and the anionic surfactant (sodium) on water exudation and wetting stages. Moreover, Mi et al. (2023) conducted injection tests at the Mengcun and Dafoxi collieries in the Binchang mining area, comparing the effects of injection pressure on displacement-effective radii and CH4 recovery. These studies address fluid injection at the laboratory and field scales, while multi-scale integrated characterization remains limited. Laboratory experiments typically focus on microscopic mechanisms of water transport at the sample scale and often do not fully consider the modification of the seepage structure by engineering boreholes. Conversely, field tests reflect macroscopic injection performance but are unable to resolve microscopic behaviors within the PFS. Thus, to deepen our understanding of coalbed injection mechanisms, it is critical to develop a multi-scale approach that integrates borehole engineering effects with fine-scale laboratory observation.

For characterizing PFS and monitoring fluid transport, researchers have developed key techniques such as nuclear magnetic resonance (NMR), X-ray computed tomography (CT), and mercury intrusion porosimetry (MIP). For example, Yang et al. (2023) used NMR to dynamically monitor online water injection in coal samples with different fracture structures. Chen et al. (2022) reconstructed three-dimensional fracture networks from CT data to achieve the quantitative and visualized characterization of pores and fractures. Jiang et al. (2019) employed MIP to obtain nanometer-scale pore distribution characteristics. However, each method has strengths and limitations: NMR offers full-scale, non-destructive online monitoring, whereas its spatial resolution and imaging intuitiveness are inferior to CT three-dimensional (3D) reconstructions (Wang et al., 2020); CT excels in visualization but struggles to capture micro- to nanoscale pores (Yu et al., 2022); MIP quantitatively characterizes pore structure and connectivity but cannot observe dynamic processes in real time (Gao et al., 2018; Yao et al., 2019). Therefore, no single optimal method exists that can comprehensively capture the complex behavior of water transport in borehole coal. Besides, existing studies largely concentrate on injection and storage stages, with relatively less attention to evaporation and loss under deep, high-temperature conditions.

To address the above need, this study integrates NMR, CT scanning and MIP to build a multi-method, collaborative analytical framework that leverages the full-scale online monitoring ability of NMR, three-dimensional visualization by CT, and the quantitative accuracy of MIP for seepage parameters. From whole-sample to layered measurements and through multi-source data fusion and mutual validation, this study performs systematic analyses from bulk properties to local regions and from static structure to dynamic processes, thereby revealing the control mechanisms of borehole treatment on injection behavior. To better reflect real engineering conditions, beyond injection experiments, this study conducts evaporation tests of saturated samples under simulated high-temperature conditions, thus linking the entire “injection-migration-evaporation” sequence. This approach systematically unveils the dynamic water transport pathways in borehole coal samples and their multi-scale PFS controls, with the objective to provide theoretical foundations and experimental support for optimizing coalbed water-injection strategies under deep, high-temperature environments.

2. Experimental design

2.1 Samples

Coal samples originated from the Dongsheng Coalfield in Inner Mongolia, China. Borehole temperature measurements indicated that the geothermal gradient in this region ranges from 1.72 to 2.47 °C/100 m. The results of the proximate analysis are shown in Table 1. Cylindrical specimens with dimensions of 25 mm in diameter and 50 mm in length were cored along the bedding direction of the raw coal. A drilling

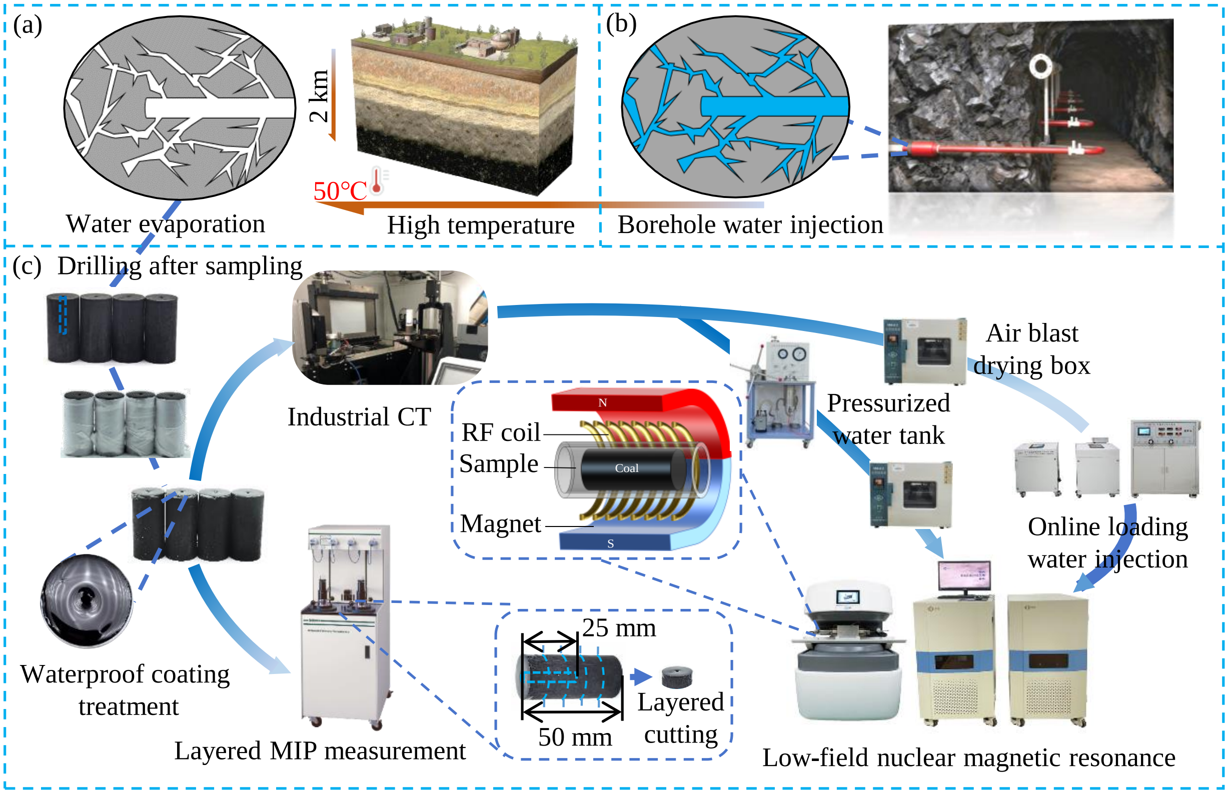

Fig. 1. Diagram of the experimental design: (a) Schematic of deep high-temperature environment, (b) schematic of coal seam borehole water injection and (c) experimental flowchart.

device was used to pre-drill boreholes with a diameter of 2 mm and a depth of 25 mm in the center of each specimen. To satisfy the requirements of the borehole water-injection experiments and to ensure that water contacted the frontal surface only through the borehole channel, the front end of each sample was coated with a waterproof layer made of epoxy resin. After natural air-drying, an effective impermeable barrier was formed, as shown in Fig. 1(c) (Zhu et al., 2023).

2.2 Experimental apparatus

CT scanning was performed using an ACTIS300-320/225 high-resolution industrial CT/DR imaging system for micro-CT analysis, with a voxel size of 30 μm (Ju et al., 2021). The NMR experiments were conducted using a MacroMR12-150H system equipped with an online water-injection and triaxial loading device (Zhou et al., 2025). Fluorinated fluid (FC-40) was used as the hydraulic medium and a pressure chamber made from titanium alloy and ceramic materials. MIP measurements were carried out using a Corelab CMS300 and an AutoPore IV 9505 mercury porosimeter (USA), with a maximum applied pressure of 200 MPa.

2.3 Experimental procedure

As illustrated in Fig. 1, the experimental program was designed to investigate the evolution of water injection, migration and subsequent evaporation loss in the borehole coal samples after saturation. The specimens were divided into a water-injection group (a1, a2, a3) and an evaporation group (e1, e2, e3). To achieve a multi-scale characterization of water invasion and transport within the coal matrix, NMR, CT scanning and MIP were employed in combination. The experimental procedures are detailed as follows:

1) After waterproof treatment of the borehole coal samples, micro-CT scanning was conducted using the ACTIS300-320/225 high-resolution industrial CT/DR system. The acquired images were reconstructed into three-dimensional models using AVIZO software.
2) The water-injection group samples (a1, a2, a3) were dried at 105 °C until a constant mass was achieved. Subsequently, each specimen was wrapped with heat-shrink tubing and fixed in the NMR online triaxial loading device. Water-injection experiments were carried out under a confining pressure of 10 MPa and an injection pressure of 2 MPa. The temporal evolution of the internal T_2 spectra and NMR imaging (NMRI) were recorded at preset time intervals during the injection process.
3) Samples in the evaporation group (e1, e2, e3) were placed in a vacuum pressurized saturation system, fully immersed in the core chamber, evacuated, and then subjected to a water pressure of 15 MPa for 24 h to ensure complete saturation (Zhou et al., 2025). After saturation, samples were transferred to a drying oven maintained at 50 °C for continuous evaporation. The evolution of the internal T_2 spectra and NMRI data was monitored and recorded at designated time points.
4) Sample a2 from the water-injection group was selected

and divided by wire cutting into five sub-samples (a2-1 to a2-5) with equal spacing along the axial direction. After drying, the sub-samples were placed in the low-pressure chamber of the mercury porosimeter and evacuated to a fully degassed state, followed by MIP testing. The obtained data were processed and analyzed to determine pore-size distributions and other relevant structural parameters.

3. Results and analysis

3.1 Integrated characterization of the PFS of borehole coal samples

3.1.1 Characterization of overall pore-size distribution

MIP is based on the capillary bundle model, which idealizes a porous medium as an assemblage of capillaries with different diameters. In this framework, the solid surface of the rock is considered as the non-wetting phase, whereas the gas phase (air or mercury vapor) occupying the pore space is regarded as the wetting phase. During the experiment, mercury intrusion represents a process in which the non-wetting phase displaces the wetting phase, i.e., mercury is progressively forced into the pore system of the rock. Therefore, by measuring the relationship between cumulative mercury intrusion volume and applied pressure, the key parameters characterizing the pore structure of coal can be quantitatively determined. When the mercury intrusion pressure is P_c, the maximum pore radius accessible to mercury will be r_c.

For hydrogen nuclei in NMR, the response time associated with transitions induced by radio-frequency pulses in a magnetic field is defined as the transverse relaxation time, T_2 (Liu et al., 2021; Manakov et al., 2024). After coal samples are fully saturated, hydrogen nuclei in water confined within pores of different sizes exhibit distinct T_2 relaxation behaviors due to variations in surface interactions and confinement effects. Consequently, the distribution of hydrogen nuclei corresponding to different T_2 values can be used to infer the pore-size distribution of the coal, thereby reflecting its internal pore structure (Liu et al., 2026).

The principle of T_2 measurements has been detailed in the classical work of Kenyon (1997). In practice, the Carr-Purcell-Meiboom-Gill pulse sequence is commonly employed to measure the T_2 relaxation time and the associated signal amplitudes (Ouyang et al., 2016). The relaxation characteristics can be described by the following equation:

$$\frac{1}{T_2} \approx \rho_2 \frac{S}{V} = F_s \frac{\rho_2}{r} \tag{1}$$

where T_2 denotes the transverse surface relaxation time, ms; ρ_2 denotes the transverse surface relaxivity, nm·ms^{-1}; S denotes the pore surface area, nm^2; V denotes the fluid volume, nm^3; r denotes the pore radius, nm; and F_S is a geometric factor. Accordingly, a fixed correspondence exists between the T_2 value and pore size: Larger T_2 values indicate larger pore radii. Moreover, a higher NMR imaging signal intensity implies a greater abundance of pores with the corresponding radius (Kenyon, 1997; Zhou et al., 2025). Fig. 2 presents the T_2 spectrum and the cumulative water saturation curve obtained for the water-injected coal sample a2 under saturated conditions. It is observed that with increasing T_2, the signal intensity exhibits multiple distinct peaks, indicating pronounced differences in pore distribution across different pore size ranges.

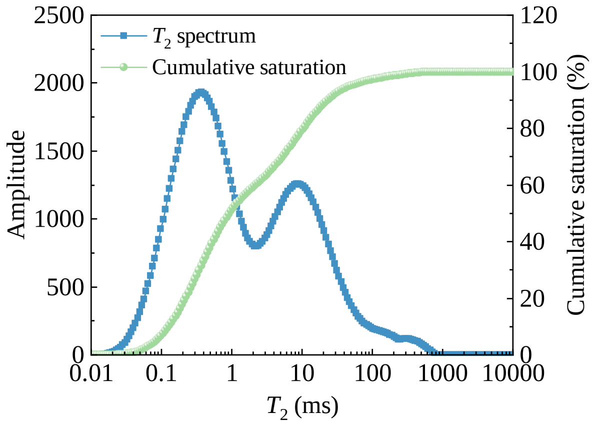

Fig. 2. T_2 spectrum and cumulative water-saturation components of coal sample a2 under water-saturated conditions.

To better characterize the PFS, the ρ_2 of the coal matrix was determined by integrating the NMR data with the mercury intrusion results. In NMR studies, the T_2 distribution of fully saturated rocks directly reflects their pore size distribution. The critical parameter linking the two is the ρ_2, a proportionality constant that characterizes the strength of surface-induced transverse relaxation at the solid-liquid interface (Ge et al., 2021). By correlating the T_2 spectrum with the PFS obtained from mercury intrusion or gas adsorption experiments, the transverse surface relaxivity can be determined (Zheng et al., 2019). Moreover, using corrected mercury intrusion data that more accurately represents the pore structure enables an improved estimation of NMR relaxation rates and, consequently, enhances the precision of NMR measurements. Based on the mercury intrusion volume at each applied pressure, mercury saturation components were calculated to represent the frequency of pores within specific pore-size ranges, yielding an overall MIP-derived pore-size distribution curve. In contrast, the T_2 spectrum reflects the water signal intensity associated with different relaxation times. Thus, for a fully saturated coal sample, the T_2 spectrum can be regarded as an NMR-derived pore-size distribution.

However, since MIP and NMR derived pore-size distributions differ in their underlying physical meanings, directly correlating the two distributions to determine surface relaxivity would be inappropriate. To ensure physical consistency, both pore-size distribution curves were transformed into cumulative pore-size distribution curves, which represent the percentage of cumulative pore volume within a given pore radius (r_i) relative to the total pore volume. This transformation enables a unified physical interpretation; by correlating the cumulative pore-size distribution curve obtained from MIP with that derived from NMR, ρ_2 of the coal matrix can be determined.

It should be noted that the raw capillary pressure curves obtained from MIP do not account for the effects of the surface cavity effect and matrix compressibility. As illustrated in Fig.

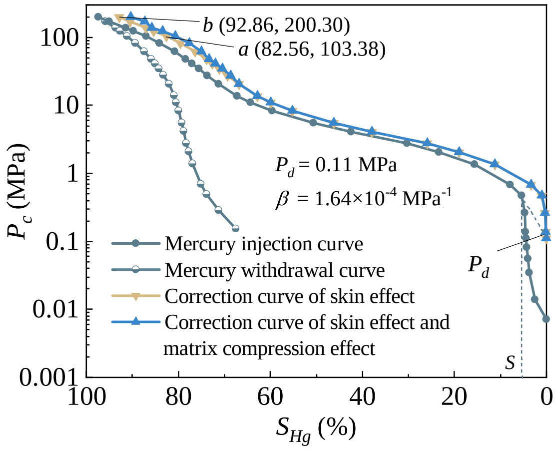

Fig. 3. Mercury intrusion curves corrected for surface cavity effect and matrix compressibility.

3, the displacement pressure (P_d) is determined by extending the relatively flat middle segment of the capillary pressure curve (dashed line in Fig. 3) to intersect the ordinate at zero mercury saturation, and this intersection is taken as P_d.

When the intrusion pressure is lower than the displacement pressure, a sudden increase in mercury saturation is observed. As the intrusion pressure continues to increase beyond P_d, the curve gradually becomes smoother and the growth rate of mercury saturation decreases. The mercury intrusion curves are corrected according to Eq. (2) by subtracting Pd from the intrusion pressure for each data point. Taking the calculated displacement pressure as a basis, the original mercury intrusion pressure curve is corrected for the surface cavity effect, yielding the surface cavity effect-corrected intrusion curve shown in Fig. 3. The results indicate that, if not corrected, the surface cavity effect can lead to an overestimation of pore volume:

$$P_{ca} = P_{cb} - P_d \tag{2}$$

where P_{ca} denotes the corrected intrusion pressure, MPa; P_{cb} denotes the original intrusion pressure, MPa; and P_d denotes the displacement pressure, MPa. In addition, at relatively high intrusion pressures, mercury may not enter the pores but instead compress the coal matrix, resulting in an apparent increase in the measured intrusion volume. Consequently, the measured mercury intrusion volume consists of two components: The true pore-filling volume and the volume associated with matrix compression. This relationship can be expressed as (Leòn, 1998):

$$\Delta V_{Hg} = \Delta V_f + \Delta V_c \tag{3}$$

where ΔV_{Hg} represents the total mercury intrusion volume measured in the MIP experiment, cm^3/g; ΔV_f represents the actual volume of mercury filling the pore space, cm^3/g; and ΔV_c represents the volume associated with matrix compression deformation, cm^3/g.

Neglecting the compressibility of mercury itself, the compressibility coefficient of coal, β, can be calculated using the following expression (Li et al., 1999):

$$\beta = \frac{1}{V_c}\frac{\mathrm{d}V_c}{\mathrm{d}P_c} \tag{4}$$

where V_c denotes the volume of the coal matrix skeleton, m^3, and P_c is the mercury intrusion pressure (MPa). It should be noted that V_c includes the compressible volume of pores that cannot be intruded by mercury.

The MIP data of surface cavity effect exhibits a clear linear relationship between mercury intrusion volume and intrusion pressure in the pressure range of 103.38 to 200.30 MPa, as seen in Fig. 3. Therefore, for the high-pressure segment of the MIP data, Eq. (3) can be rewritten as:

$$\frac{\sum_b^a V_{Hg}}{\Delta P_c} \approx \frac{\sum_b^a V_f}{\Delta P_c} + \frac{\Delta V_c}{\Delta P_c} \tag{5}$$

Assuming that the compressibility coefficient of the coal matrix remains constant, Eqs. (4) and (5) can be combined to yield:

$$\beta = \frac{1}{V_c}\left(\frac{\sum_b^a V_{Hg}}{\Delta P_c} - \frac{\sum_b^a V_f}{\Delta P_c}\right) \tag{6}$$

Li et al. (2021) found that, after compressibility correction, the pore volume corresponding to the mercury intrusion pressure range of 103.38 to 200.30 MPa is very small and can be neglected. Therefore, Eq. (6) can be simplified as:

$$\beta = \frac{1}{V_c}\frac{\sum_b^a V_{Hg}}{\Delta P_c} \tag{7}$$

On the basis of the compressibility of the coal matrix, the pore volume at any mercury intrusion pressure (P_{ci}) can be expressed as:

$$\begin{aligned} V_f(P_{ci}) = {} & V_f P_{c(i-1)} + V_{Hg} P_{ci} - V_{Hg} P_{c(i-1)} - \\ & \beta\left(V_{bulk} - V_{Hg} P_{c(i-1)}\right)\left(P_{ci} - P_{c(i-1)}\right) \end{aligned} \tag{8}$$

where P_{ci} and $P_{c(i-1)}$ represent the mercury intrusion pressures at points i and $i-1$, respectively, MPa; $V_f(P_{ci})$ and $V_f(P_{c(i-1)})$ are the corresponding pore volumes at these pressure points, cm^3; $V_{Hg}(P_{ci})$ and $V_{Hg}(P_{c(i-1)})$ denote the measured mercury intrusion volumes at points i and $i-1$, cm^3; and V_{bulk} is the bulk volume of the sample, cm^3.

Using Eqs. (7) and (8), the capillary pressure curve for mercury intrusion pressures above 20 MPa was corrected, as shown in Fig. 3, representing the mercury intrusion pressure after accounting for both the surface cavity effect and matrix compressibility. Table 2 presents a comparison of porosity parameters of coal sample a2 before and after correction of the mercury intrusion curve. This correction effectively eliminates the overestimation of pore volume and provides a more rigorous and accurate basis for determining the ρ_2 from NMR measurements.

Based on Eq. (1), the relationship between NMR-derived pore radius and mercury intrusion pressure was established. The ρ_2 was then determined by achieving the best match between the cumulative pore-size distribution curves obtained from NMR and the corrected MIP data. First, cumulative saturation curves were plotted on the same coordinate system for the NMR T_2 spectra under different ρ_2 values and the corrected mercury intrusion curve. Then, based on the principle of maximum similarity and using the least-squares method,

Table 2. Parameters of sample a2 before and after correction of MIP.

Parameter	Porosity (%)	Pore-throat radius (μm)		
		Mean	Median	Maximum
Pre-correction	15.13	0.026	0.134	102.14
Post-correction	14.42	0.267	0.110	6.66

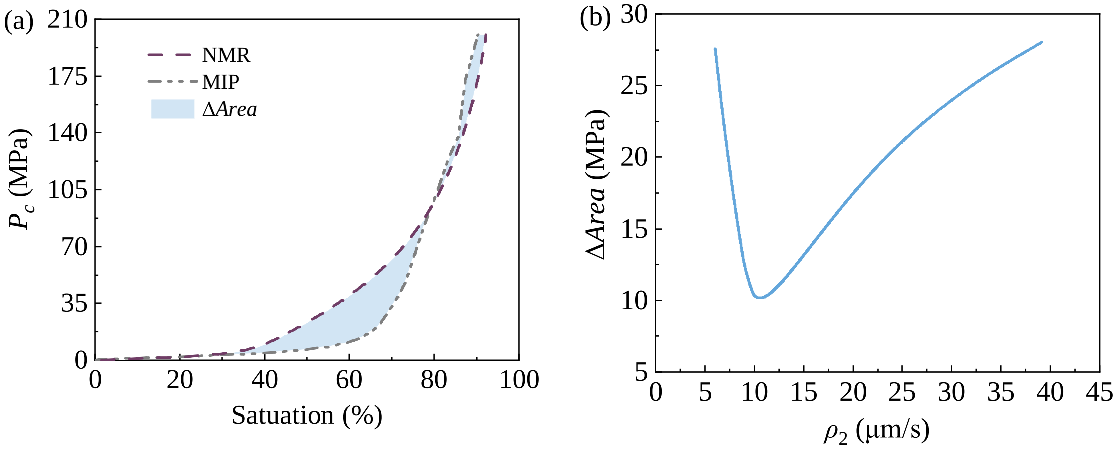

Fig. 4. Normalization of NMR and MIP data and determination of optimal transverse surface relaxivity: (a) Associated area and (b) ρ_2 evolution.

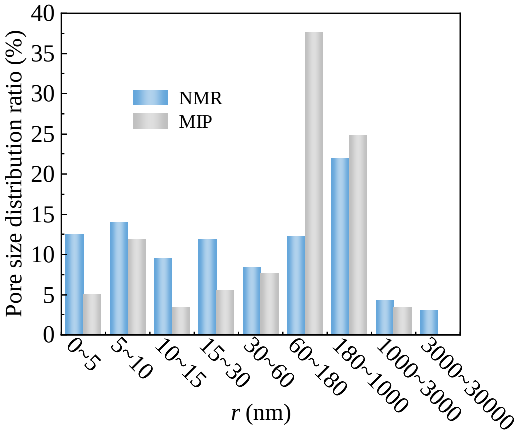

Fig. 5. Comparison of pore-size distributions obtained from NMR and MIP for coal sample a2.

the error between the two curves for each ρ_2 value was calculated, represented by the area enclosed between the curves (Fig. 4). The ρ_2 value corresponding to the minimum error was taken as the optimal transverse surface relaxivity.

By substituting the calculated ρ_2 into Eq. (3), the transverse relaxation time T_2 can be converted into pore radius, as shown in Fig. 5. Because the measurement mechanisms of NMR and MIP differ (Zhang et al., 2024; Zhou et al., 2025), the number of data points obtained from each method is not identical. To ensure that the resulting normalized pore-size fractions are not biased, the pore-size distributions from both experiments were divided into discrete pore-radius intervals before statistical comparison.

The analysis of results indicates that the sensitivity of each method to different pore size ranges varies. For coal sample a2, the NMR-derived pore-size distribution exhibits a higher proportion of pores in the smaller-size range ($<$ 60 nm) compared with MIP; conversely, in the larger pore range ($>$ 60 nm), MIP yields a higher proportion of pore distribution than NMR. This discrepancy primarily arises from the differing measurement scales of the two techniques: NMR, being non-destructive and full-sample in nature, captures water in micro- and nanoscale pores more comprehensively, whereas MIP is limited by the applied intrusion pressure, restricting its ability to access the smallest pores. As a result, compared with NMR, the proportion of micro-scale pores is relatively lower in the MIP-derived pore-size distribution.

3.1.2 Analysis of the layered PFS of coal sample

The coal samples were subjected to incomplete borehole treatment, as shown in Fig. 1(c). To analyze the impact of borehole disturbance on the coal, the samples were measured in a stratified manner, allowing the comparison of PFS between the borehole-affected region and the non-borehole region.

The mercury intrusion-extrusion curves were obtained for different stratified positions of the coal sample. From these curves in Fig. 6(a), the MIP-derived parameters listed in Table 3 were calculated. Substituting the data into Eq. (9) yields

Table 3. MIP measurement parameters and geometric mean values of NMR T_2 spectra.

No.	K (10^{-3}μm^2)	ϕ (%)	R_p (μm)	T_{2g} (ms)	S_p (-)	ϕ_p (-)	D_r (-)	$1/(D_r\phi_p)$ (-)
a2-1	0.723	15.67	0.287	7.532	2.722	2.224	10.38	0.043
a2-2	0.666	15.63	0.281	7.542	2.713	2.311	10.93	0.040
a2-3	0.637	16.03	0.270	7.043	2.711	2.291	11.256	0.039
a2-4	0.531	14.71	0.263	6.457	2.686	2.387	11.904	0.035
a2-5	0.542	15.05	0.262	6.581	2.729	2.387	12.114	0.035

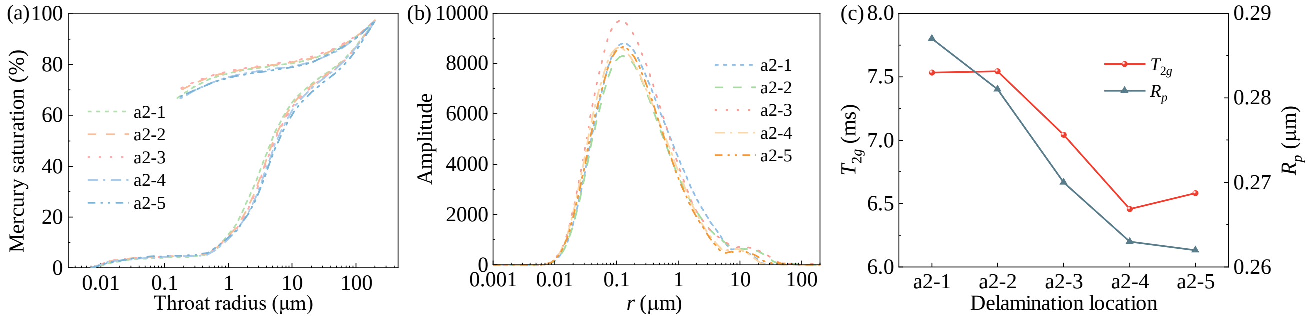

Fig. 6. Layered pore-fracture structure measurements and parameter evolution of coal sample a2: (a) MIP intrusion-extrusion curves, (b) NMR T_2 spectra and (c) T_2 geometric mean values and MIP average pore radius.

the structural coefficient ϕ_p, which characterizes the deviation between the actual pore structure of the coal and the idealized model of parallel cylindrical capillaries with equal length but varying diameter.

Substituting the data into Eq. (10) provides the relative sorting coefficient D_r, which better reflects the uniformity of pore-throat size distribution. Smaller D_r values indicate a more uniform pore-throat distribution. The reciprocal of the product of D_r and ϕ_p is defined as the characteristic structural coefficient, which quantifies the combined effects of multiple factors influencing the pore structure differences. This parameter reflects both the degree of pore-throat sorting and the connectivity of the network: The smaller its value, the poorer the PFS of the coal sample:

$$\phi_p = \frac{\phi}{8K} R_p^2 \tag{9}$$

$$D_r = \frac{S_p}{R_p} = \frac{1}{R_p}\sqrt{\frac{\sum (r_i - R_p)^2 \times \Delta S_i}{\sum \Delta S_i}} \tag{10}$$

where ϕ_p denotes the structural coefficient; R_p denotes the average pore-throat radius, μm; ϕ is the porosity, %; K denotes the air permeability, μm^2; D_r denotes the relative sorting coefficient; S_p denotes the sorting coefficient; r_i denotes the pore-throat radius at a given point, μm; and ΔS_i is the mercury saturation corresponding to the interval around r_i, %.

Next, the stratified NMR measurements of the saturated coal sample were performed. By substituting the T_2 spectra into Eq. (11), the geometric mean relaxation time (T_{2g}) was obtained, as shown in Fig. 6(b), which characterizes the evolution of average pore size in different stratified layers (Kenyon et al., 1988):

$$\sqrt[m]{T_{2g}} = \prod_{t=1}^{m} T_{2t}^{A_t} \tag{11}$$

where A_t represents the amplitude of the t measured T_2 data point, indicating the ratio of the signal intensity at relaxation time T_{2t} to the total signal intensity; and m is the total number of T_2 data points collected during the measurement.

By comparing the stratified NMR and MIP measurements, a consistent qualitative trend can be observed across different layers in terms of pore-throat size, permeability and related parameters: Borehole-affected regions (a2-1, a2-2) > partially borehole-affected region (a2-3) > non-borehole regions (a2-4, a2-5). This trend indicates that borehole disturbance not only promotes the development of pore and fracture sizes but also enhances connectivity between pore throats, thereby optimizing the flow pathways within the overall PFS. Furthermore, the deeper the borehole penetration is, the greater the disturbance, resulting in a more pronounced improvement in the permeability of the PFS.

3.1.3 Characterization of the overall PFS of coal samples

Next, a comparison between NMRI and CT-based 3D reconstructions was performed for the saturated coal sample. As shown in Fig. 7, during the measurement, a phase-encoding gradient is first applied and then removed, followed by the application of a frequency-encoding gradient, which links the frequency information to spatial position, allowing the acquisition of NMR signal intensity at different locations within

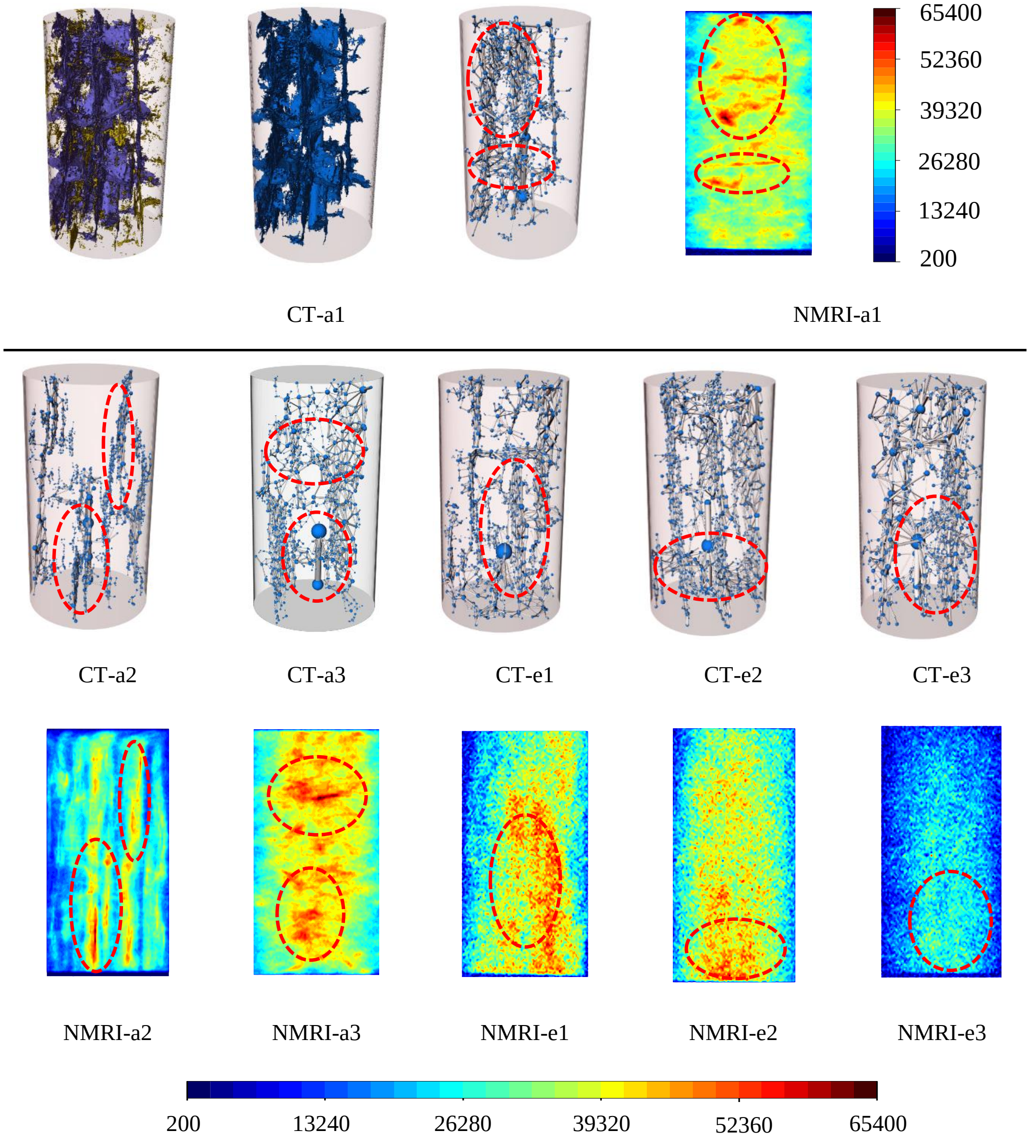

Fig. 7. Comparison of 3D CT stick-and-ball reconstruction and two-dimensional NMRI.

the sample. Finally, through denoising, decoding and image reconstruction steps, the NMRI provides a three-dimensional representation of the spatial distribution of the PFS in the coal sample. This approach complements CT imaging by capturing the fine-scale, water-filled pores that may not be resolved in the CT scans, enabling a comprehensive characterization of the overall PFS of coal after borehole treatment.

From the NMRI data, it can be observed that, compared with samples a1 and a3, coal sample a2 exhibits more independent bedding planes with fewer interconnected channels between layers. Similarly, sample e3 shows a more dispersed pore distribution compared with e1 and e2. However, since NMRI provides a two-dimensional superimposed structural view, it can only qualitatively indicate the general differences between coal samples. To verify these observations more directly and quantitatively, the CT scan data were reconstructed in 3D. The CT images were first binarized using the Triangle algorithm embedded in ImageJ to segment the PFS from the coal matrix at the resolvable CT scale. Next, the thresholded images were imported into AVIZO, where AXIS CONNECTIVITY analysis was utilized to distinguish connected pores from isolated pores. All extracted pore structures, regardless of their original shapes, were simplified as equivalent spheres, and the equivalent pore diameter was used to represent the pore size:

$$D_e = \sqrt[3]{\frac{6V_e}{\pi}} \tag{12}$$

where D_e represents the equivalent pore diameter, μm; and V_e is the volume of a single pore, μm^3.

Using the connected pore extraction module in AVIZO, a model of connected pores penetrating along a specific coordinate axis was obtained, representing pathways through which fluid can flow in that direction. Pores were classified into isolated pores and connected pores. To analyze the contribution of different pore types to the total porosity (ϕ), porosity

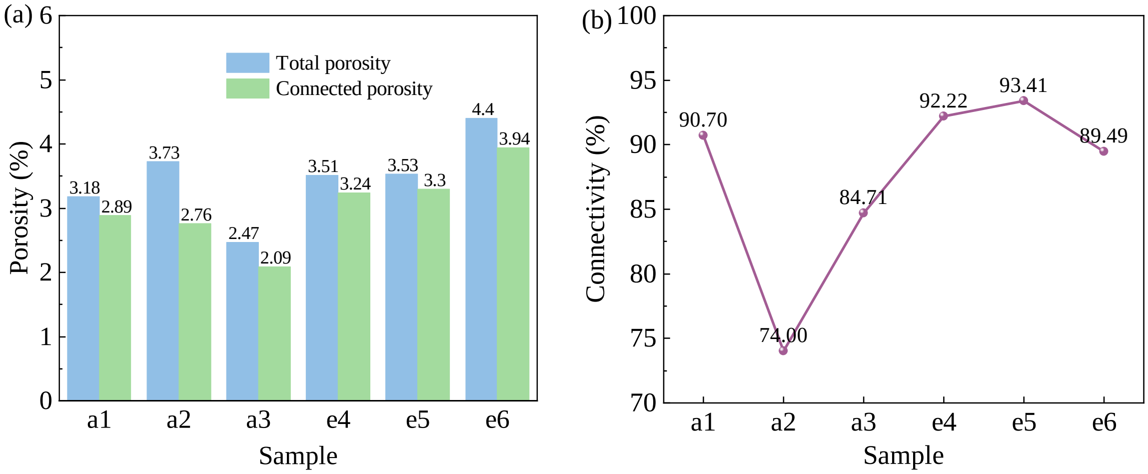

Fig. 8. CT-based reconstruction showing the calculated porosity and connectivity of pores: (a) Comparison of pore structure classifications in coal samples and (b) connectivity of coal samples.

Table 4. CT-based calculation of porosity and connectivity.

No.	T_c (%)	Porosity component (%)		
		ϕ_{dp}	ϕ_{cp}	ϕ
a1	90.70	0.30	2.89	3.18
a2	74.00	0.97	2.76	3.73
a3	84.71	0.38	2.09	2.47
e1	92.22	0.27	3.24	3.51
e2	93.41	0.23	3.30	3.53
e3	89.49	0.46	3.94	4.40

is defined as the ratio of the volume of a specific pore category to the total volume of the coal sample:

$$\phi_{dp} = \frac{V_{dp}}{V} \tag{13}$$

$$\phi_{cp} = \frac{V_{cp}}{V} \tag{14}$$

where ϕ_{dp} and ϕ_{cp} respectively represent the porosity fractions of isolated pores and connected pores, %; V_{dp} and V_{cp} respectively represent the total volumes of isolated pores and connected pores, μm^3; and V is the total volume of the coal sample, μm^3.

Connectivity is defined as the ratio of the connected pore volume to the total pore volume:

$$T_c = \frac{V_{cp}}{V_p} \tag{15}$$

where T_c denotes the pore connectivity, % and V_p is the total pore volume, μm^3.

Fig. 8 presents the comparison of porosity and connectivity calculated from 3D CT reconstructions, with the detailed numerical values listed in Table 4. The analysis of 3D views reveals the following trends for the water-saturated coal samples (a1, a2, a3): Firstly, coal sample a2 exhibits the lowest connectivity, at 74.00%. The 3D reconstruction shows relatively independent bedding planes with few laterally connected channels. Secondly, coal sample a1 has the highest connectivity at 90.70%, followed by a3 at 84.71%. In a1 and a3, numerous lateral connections exist between bedding planes, and some layers are directly connected to the borehole via primary flow channels, allowing water to rapidly reach inter-layer voids. Finally, regarding connected porosity (ϕ_{cp}), the trend is a1 (2.89%) > a2 (2.76%) > a3 (2.09%). Notably, although a2 has a higher total porosity than a1, its connected pore volume falls between a1 and a3.

The same comparison for the evaporated samples (e1, e2, e3) shows the following trends: Firstly, the connectivity follows the order is a2 (93.41%) > a1 (92.22%) > a3 (89.49%). Secondly, from the CT 3D reconstructions, sample e3 shows a more dispersed pore-fracture distribution, with isolated pores reaching 0.46%, accounting for 10.51% of total porosity (higher than in e1 and e2). Finally, e1 and e2 display more uniform vertical bedding distribution, with well-developed lateral connectivity between layers.

3.2 Evolution of water migration under pressurized injection

3.2.1 Overall evolution

The water injection process was monitored online using NMR equipment. Fig. 9(a) shows the evolution of water infiltration in coal samples a1, a2, and a3 as a function of injection time, where the horizontal axis represents injection time, while the vertical axis represents cumulative injected water volume. The injection process can be divided into two stages: An initial rapid increase in water volume, followed by a slower growth stage as injection progresses.

Next, the PFS was further classified and analyzed. Figs. 9(b) and 9(c) show the evolution of the T_2 spectra and cumula-

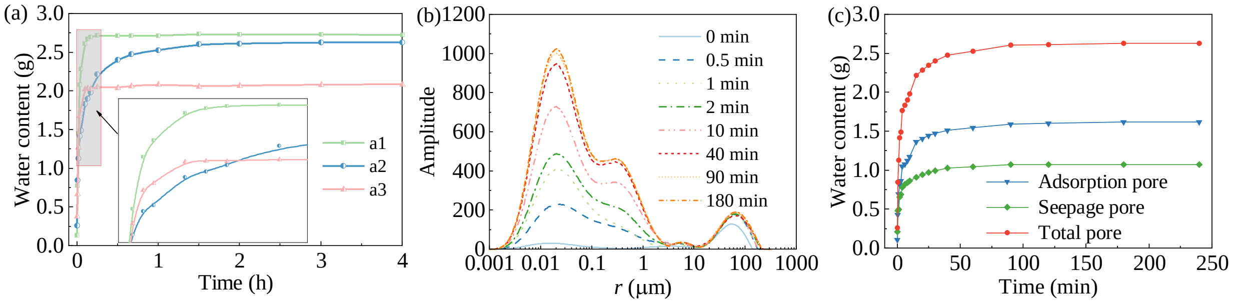

Fig. 9. Evolution of water migration during water injection: (a) Comparison of water injection behavior, (b) evolution of the T_2 spectra of a2 and (c) water injection process within different pore categories of a2.

tive signal intensity for coal sample a2 during injection. Based on the textbook 'Coal and Gas Outbursts' by Hodot (1966), pores of different sizes play distinct spatial roles. Therefore, a threshold of 100 nm was adopted to distinguish micropores (adsorption space) from mesopores and macropores (seepage space), and the cumulative signal intensity was tracked for each category. The results indicate that seepage pores reach a stable water content more quickly than adsorption pores, primarily because their larger diameters allow faster contact with injected water via borehole channels. In contrast, adsorption pores rely on capillary forces for water uptake. However, in the fully saturated state, adsorption pores hold a larger fraction of water, with a contribution up to 63.75%, due to their higher porosity than seepage pores.

Notably, under identical injection conditions, samples a1 and a3 reach stability earlier, while a2 exhibits a slower initial injection rate. Nevertheless, at the final stabilized stage, the total water content in a3 is lower than that in a1 and a2. This phenomenon can be explained by the combined NMRI and CT analysis discussed in Section 3.1.3. Sample a2 possesses the lowest connectivity (74.00%), characterized by relatively independent bedding planes and fewer lateral channels. In contrast, sample a1 exhibits the highest connectivity (90.70%), followed by a3 (84.71%). In both a1 and a3, numerous lateral connections exist between bedding planes, and some layers are directly connected to the borehole through primary flow channels, enabling rapid water transport into inter-layer voids, which explains the observed trend in injection rate, namely a1 > a3 > a2. With respect to connected porosity (ϕ_{cp}), a3 shows the lowest value (2.09%), followed by a2 (2.76%), while a1 has the highest value (2.89%). The ranking of connected porosity is consistent with the ranking of the final injected water volume, indicating that connected porosity is the key parameter controlling the maximum injectable water capacity.

In summary, the analysis shows that injection efficiency in the early stage is primarily governed by the connectivity of the seepage network: Samples with higher connectivity and more developed lateral inter-layer channels allow faster water penetration; by contrast, the final injectable water volume is mainly determined by connected porosity, meaning that even under identical injection conditions, samples with lower connected porosity ultimately retain less water. Therefore, a comprehensive evaluation of coal sample water-injection performance should consider both connectivity and connected porosity, as they jointly reflect the dynamic infiltration behavior and the final water-storage capacity.

3.2.2 Layered evolution during pressurized water injection

To better elucidate the influence of drilling treatment on the water injection process, a combined MIP-NMR analytical approach was adopted. Coal sample a2 was divided along the drilling direction into five sublayers: a2-1 to a2-5. Among them, a2-1 and a2-2 correspond to the fully drilled-through regions, a2-3 represents the partially drilled region, while a2-4 and a2-5 denote the non-drilled regions.

As shown in the layered T_2 evolution map (Fig. 10), the a2-1 and a2-2 regions exhibit a pronounced increase in NMR signal intensity immediately after water injection begins. The signals tend to stabilize after approximately 3 min, indicating that the drilled-through zones rapidly establish effective hydraulic connectivity with the injected water. In contrast, the a2-3 region shows a relatively slower increase in signal intensity, with more time required to reach a stable injection state. The a2-4 and a2-5 regions display the lowest injection efficiency, characterized by slow signal growth and the longest time needed to reach stabilization. The layered comparison clearly demonstrates that drilling treatment significantly enhances the water injection efficiency of coal samples, and a greater drilling depth leads to a more pronounced improvement in injection efficiency.

By integrating the layered MIP and NMR results, it can be inferred that drilling-induced water injection creates direct hydraulic contact between the coal matrix and the water source, thereby substantially shortening the transport path for water migration. As the drilling depth increases, the affected volume of the coal expands and more effective interlayer seepage pathways are formed, which in turn facilitates rapid water invasion and layered diffusion within the coal seam.

3.3 Evolution of water migration under high temperature

3.3.1 Overall evolution during high-temperature evaporation

To more intuitively analyze the evolution of moisture loss, Fig. 11(a) compares the evaporation rate differences of the

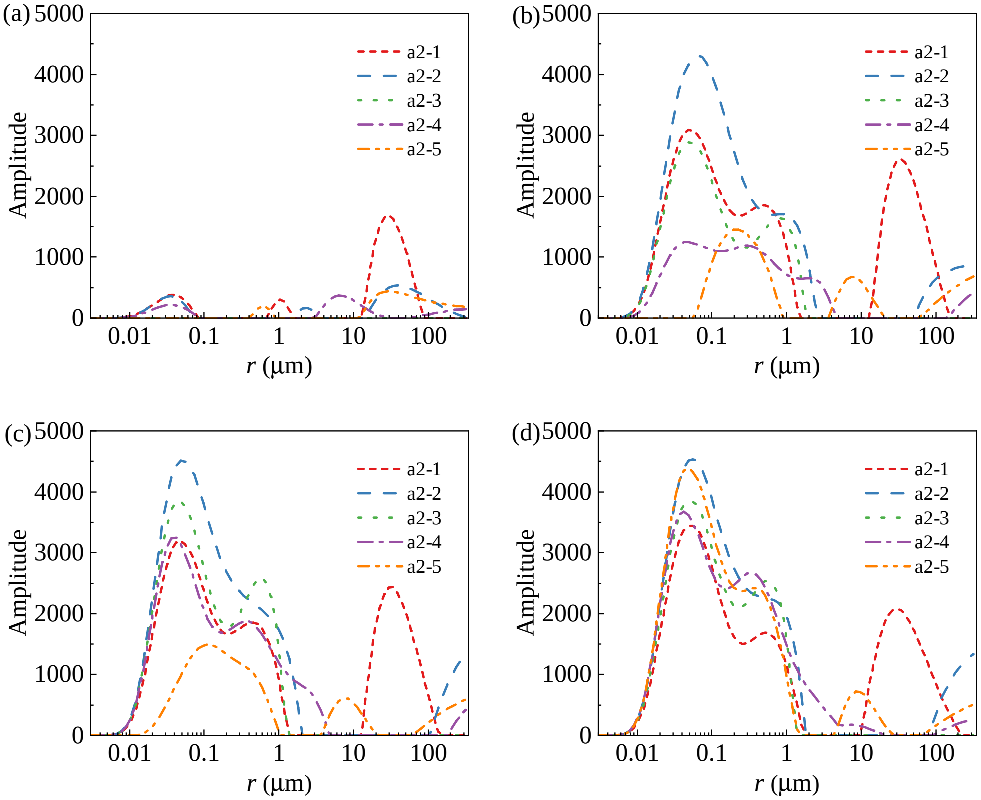

Fig. 10. Layered NMR measurements of water injection evolution in coal sample a2 at (a) 0 min, (b) 3 min, (c) 10 min and (d) 60 min.

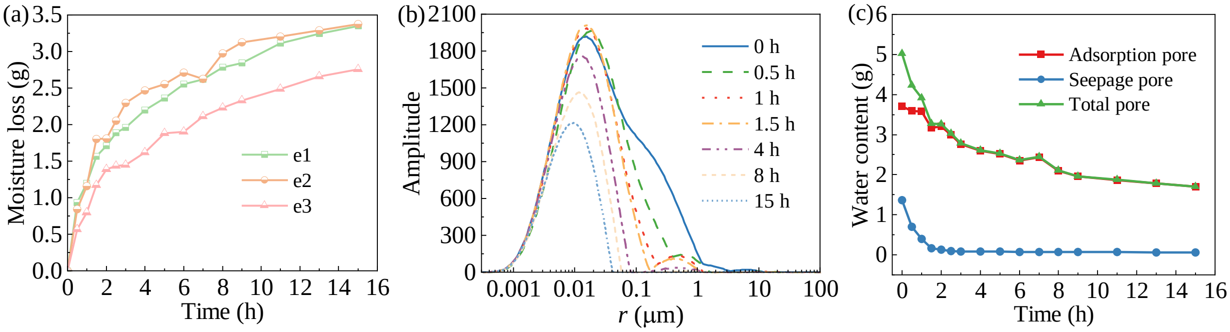

Fig. 11. Evolution of internal water evaporation: (a) Comparison of overall internal water-loss evolution, (b) evolution of the T_2 spectrum of e2 during the water-loss process and (c) water-loss processes within different pore-size classes of e2.

three coal samples using the ratio method. It can be seen that sample e3 exhibits a slower evaporation rate than e1 and e_2 (e2 > e1 > e3). By combining the CT three-dimensional reconstructed images shown in Fig. 7 with the porosity parameters listed in Table 3, the internal PFS of the coal samples can be analyzed. The CT reconstructions indicate that sample e3 has a more dispersed PFS distribution, with an isolated pore content of 0.46% and a pore connectivity of 89.49%, which is lower than that of e1 (92.22%) and e2 (93.41%). This suggests that a higher pore connectivity and a larger proportion of connected pores provide more natural transport pathways and more diverse migration routes under natural conditions, which are more favorable for gas volatilization and migration.

Subsequently, the PFS was further classified and analyzed. Figs. 11(b) and 11(c) present the evolution of T_2 spectra and the water-content variations within different pore-size classes of coal sample e_2 during internal water migration and loss under an environmental temperature of 50 °C. The results reveal the following trends in water migration within the PFS: The overall water content is mainly contributed by adsorption-dominated pore spaces. As time progresses, free water in the seepage (percolation) pores is preferentially lost. Consequently, the evolution curve of the total water content in the coal gradually converges with that of the adsorption pores,

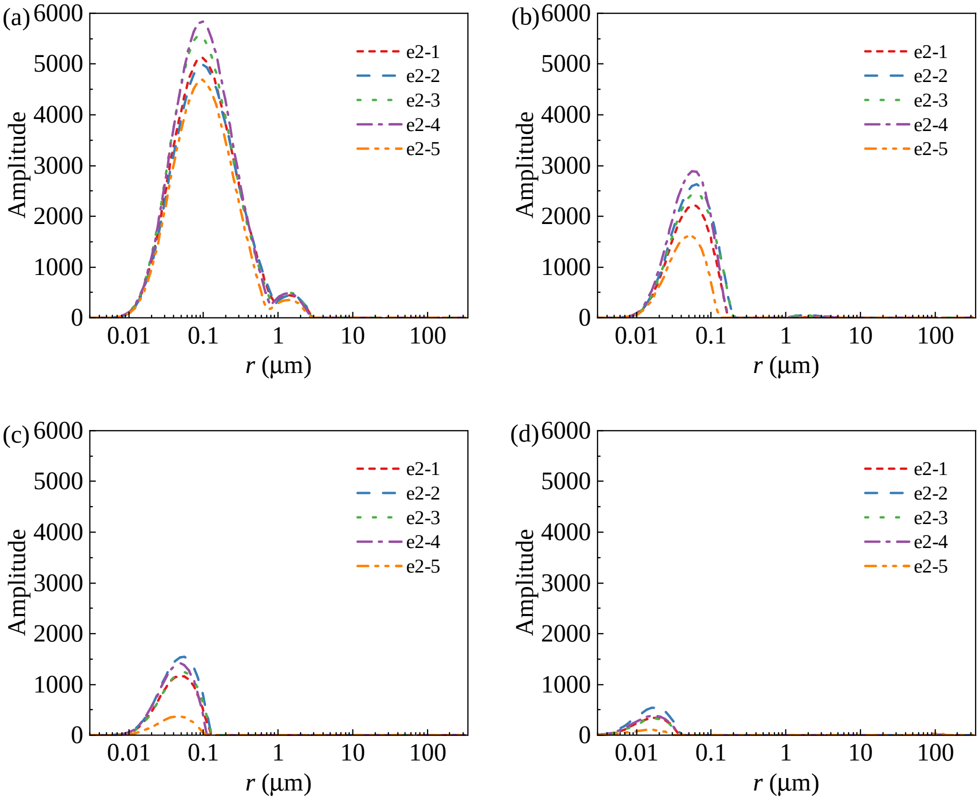

Fig. 12. Layered NMR measurements of water-loss evolution in coal sample e2: (a) 0 h, (b) 3 h, (c) 7 h and (d) 15 h.

indicating that water retained in adsorption pores progressively becomes the dominant fraction of the remaining water. As time further progresses, this adsorbed water continues to be lost, but at a significantly reduced rate. These observations indicate that during water-loss processes under high-temperature conditions, water in coal migrates predominantly in the gaseous state. Water in seepage pores is exhausted first, followed by the progressive loss of water from adsorption-dominated pore spaces.

3.3.2 Layered evolution during high-temperature evaporation

To investigate the influence of borehole treatment on subsequent water loss after injection in engineering scenarios, a layered T_2 scan analysis was conducted to examine differences in water evaporation. The layering definition is the same as in Section 3.2.2, dividing coal sample e2 into five sublayers: e2-1 to e2-5.

The evolution was analyzed using hierarchical data. As shown in Fig. 12, water loss is rapid during the first three hours, with a pronounced decrease in water content. In this stage, the majority of water loss occurs as evaporation of free water from large pores and fracture networks. After approximately three hours, the process transitions to a slower water-loss stage, with the rate gradually decreasing and eventually stabilizing. During this stage, the dominant component of water loss shifts from free water in larger pores to bound water in smaller micropores, which is more difficult to mobilize.

Interestingly, the differences in water loss among the various sublayers of the drilled coal sample are less pronounced compared to the injection process. Over time, water in all sublayers evaporates gradually, and the sequence and rate of water loss among layers show minimal variation. This indicates that, unlike injection, water evaporation is not significantly affected by borehole treatment. The primary reason is that water in saturated coal migrates predominantly as vapor, and gas diffusion does not preferentially follow borehole channels. The intrinsic micropore and fracture networks within the coal matrix provide sufficient pathways for water vapor to diffuse irregularly to the external environment. As a result, the differences in evaporation between drilled and non-drilled regions are negligible.

4. Discussion

4.1 Factors influencing the pressurized water injection performance

Layered T_2 analysis provides a relatively good macroscopic qualitative assessment of how drilled versus non-drilled treatments affect water injection efficiency in coal seams. Meanwhile, the microscale mechanisms by which drilling influences coal properties and water migration require further investigation. To comprehensively characterize the mechanisms by which drilling enhances water injection performance, this study combines MIP and CT, allowing the analysis of PFS connectivity, pore-throat size distribution, and spatial pathways

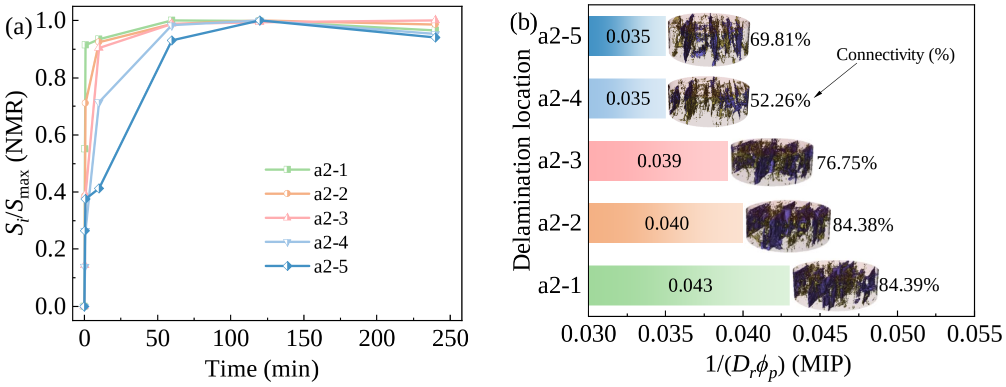

Fig. 13. Comparison of the evolution of layered data: (a) Layered evolution of water injection and (b) comparison between the MIP characteristic coefficients and CT reconstruction results.

at multiple scales. In this way, it can be revealed how drilling modifies the coal matrix and fracture networks to facilitate water penetration and optimize injection efficiency.

The analysis of pore-throat radii and characteristic structural coefficients in Table 3 shows that both the median and mean pore-throat radii follow the same trend as observed in the permeability analysis comparing drilled and non-drilled regions. This indicates that drilling disturbance promotes the development of the PFS within the coal, increasing pore sizes and enlarging seepage pathways. The characteristic structural coefficients in the drilled regions are 0.043 and 0.040, while in non-drilled regions, they are 0.035, while the value is 0.039 in the partially drilled region, lying between the drilled and non-drilled values.

Next, the data from various experimental methods were combined for integrated characterization. As shown in Fig. 13(a), the line plot represents the evolution of water content at different layers, with the vertical axis indicating the ratio of water content at any time S_i to the maximum water content $S_{\max}$. In Fig. 13(b), the inset CT images display the 3D reconstruction results for each layer, with the percentages representing the corresponding pore connectivity, and the bar chart compares the characteristic structural coefficients across layers. These trends are consistent with the layered water-injection evolution: Drilled regions show higher values, corresponding to more efficient water penetration during injection. Therefore, borehole disturbance not only promotes the enlargement of PFS sizes but also enhances connectivity between pore throats, optimizing the overall seepage network. Drilling-induced fractures enhance the pre-existing natural fracture network, with instrumentation observations indicating that the primary differences between drilled and undrilled zones are attributable to these induced fractures. Moreover, greater drilling coverage and depth amplify these effects, resulting in more pronounced improvements in the permeability of the PFS.

To better characterize the combined influence of pore-fracture development in drilled coal samples on water injection performance, a generalized model was established based on the integrated analysis of the NMR, CT and MIP experimental results. This model qualitatively represents early-stage and late-stage water injection behavior at a unified time scale, while taking into account key parameters such as PFS connectivity, internal coal porosity, and borehole treatment depth.

To more intuitively describe the mechanism underlying the influence of water injection behavior, the combined influence of coal sample porosity and connectivity on water injection performance was illustrated in a generalized model, as shown in Fig. 14. It can be seen that the overall water injection performance is jointly influenced by pore connectivity and porosity. For a clearer comparison, the model is presented on a Cartesian coordinate system, in which the horizontal axis represents porosity content and the vertical axis represents connectivity proportion, thereby dividing the injection behavior into four distinct scenarios. In Quadrant I, both connectivity and porosity are high, resulting in rapid early-stage injection rates and high final water content. In Quadrant II, porosity is high but connectivity is poor, leading to a slower initial injection rate, yet the late-stage water penetration is higher as water gradually infiltrates the coal. In Quadrant IV, connectivity is high but porosity is low, producing a fast early-stage injection but limited overall water uptake in the later stage. In Quadrant III, both connectivity and porosity are low, causing poor injection performance in both the early and late stages.

4.2 Factors influencing water loss in borehole coal samples

Based on the study of water migration and evaporation behavior in drilled coal samples, the water loss process is primarily governed by the pore-fracture structure, connectivity, and pore size distribution of the coal. To quantitatively describe the temporal evolution of water loss, an empirical exponential model was established by fitting the evaporation data as follows:

$$W = mn^t + W_0 \tag{16}$$

where W denotes the water saturation, %, W_0 denotes the initial state; m and n are fitting parameters related to the evaporation evolution; and t represents the time, h.

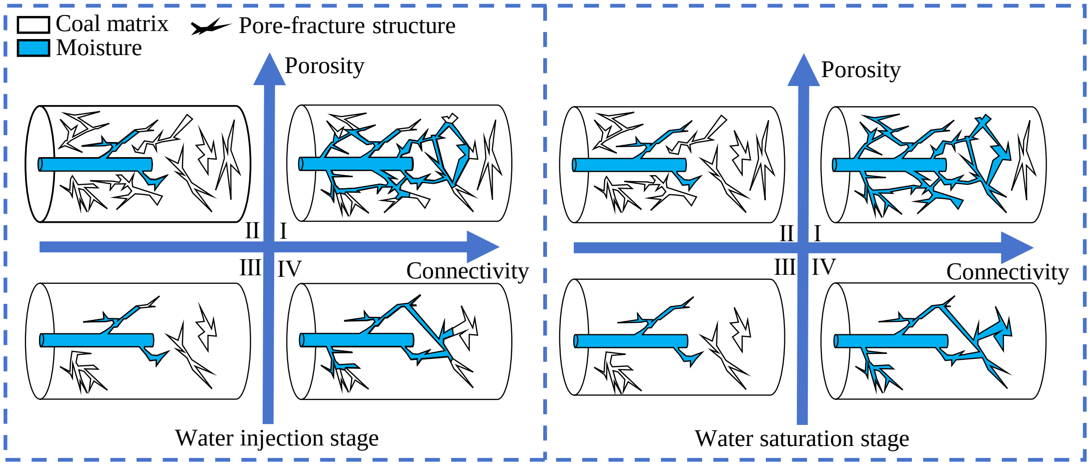

Fig. 14. Generalized model illustrating the combined influence of coal sample porosity and connectivity on water injection performance.

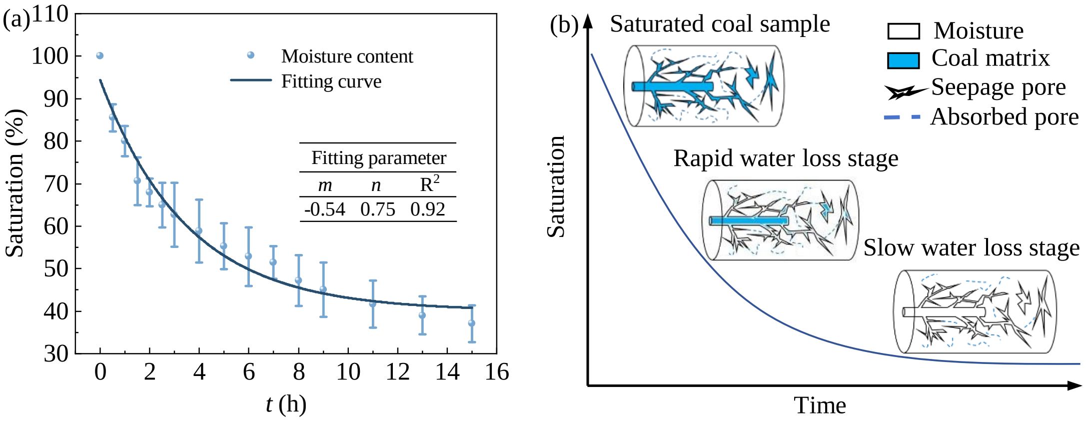

Fig. 15. (a) Model fitting results for water evaporation and (b) schematic diagram of water migration during evaporation.

The fitted results of the evaporation model indicate the general trend of water loss. As shown in Fig. 15(a), the saturation decreases exponentially with time. Based on this trend, a generalized model of internal water migration and evaporation within the PFS is proposed (Fig. 15(b)). During the entire process, water is lost primarily through thermal evaporation, and the sequence of water loss is governed by connectivity and flow pathways within the coal. Borehole interventions have little influence on water evaporation. In the early stage, water loss is dominated by free water in flow (permeable) pores, which evaporates rapidly. Water mainly diffuses as vapor, and the process is minimally affected by the macroscopic flow channel structure. In the late stage, as free water in flow pores is depleted, water in adsorption (micropore) spaces becomes exposed. Due to the narrow pore sizes and reduced connectivity, water exists primarily as bound water, making evaporation slow and the overall loss process gradual.

The above conceptual model highlights the spatiotemporal hierarchy of water migration and evaporation in borehole coal samples under high-temperature conditions. However, this model was developed based on evaporation at 50 °C, which imposes certain limitations. Future work could extend and refine the model to account for evaporation under varying temperature gradients.

5. Conclusions

The study conducts a comprehensive analysis of PFS characteristics and water migration behavior in coal samples by integrating NMR, CT and MIP measurements. The main findings are summarized as follows:

1) The analysis of NMR and CT-based 3D reconstructions reveals the spatial distribution of the PFS and pore connectivity parameters. Water injection efficiency is jointly controlled by pore connectivity, which determines the injection rate, and connected porosity, which in turn governs the maximum achievable water volume.
2) Combined MIP and NMR measurements demonstrate that NMR effectively characterizes small pores, whereas MIP captures larger pores. Borehole treatment significantly alters the coal PFS, increasing the average pore size and structural coefficients in drilled regions, thereby enhancing water injection performance.

3) Under high-temperature conditions, water loss occurs in two stages: Rapid evaporation of free water in flow pores, followed by slow desorption of bound water in adsorption pores. Higher pore connectivity accelerates evaporation rates, while borehole treatment has minimal effect on overall water loss, which is predominantly governed by diffusion through micropores rather than macroscopic pathways.

Acknowledgements

The present work has been supported by the Deep Earth Probe and Mineral Resources Exploration-National Science and Technology Major Project (No. 2024ZD1003902), the Special Project for Intergovernmental Cooperation in Scientific and Technological Innovation of National Key Research and Development Program (No. 2025YFE0109800), the National Natural Science Foundation of China (No. 52121003), and the European Commission Horizon Europe Marie Skłodowska-Curie Actions Staff Exchanges Project-LOC3G (No. 101129729).

Conflicts of interest

The authors declare no competing interest.

References

Aydin, G. Modeling of energy consumption based on economic and demographic factors: The case of Turkey with projections. Renewable and Sustainable Energy Reviews, 2014, 35: 382-389.

Chen, J., Cheng, W., Wang, G., et al. Effect of dominated coal pores and fractures on water migration after low-pressure water injection based on CT images. Fuel, 2022, 307: 121795.

Fairhurst, C. Some challenges of deep mining. Engineering, 2017, 3(4): 527-537.

Gao, F., Song, Y., Li, Z., et al. Quantitative characterization of pore connectivity using NMR and MIP: A case study of the Wangyinpu and Guanyintang shales in the Xiuwu basin, Southern China. International Journal of Coal Geology, 2018, 197: 53-65.

Ge, X., Myers, M. T., Liu, J., et al. Determining the transverse surface relaxivity of reservoir rocks: A critical review and perspective. Marine and Petroleum Geology, 2021, 126: 104934.

Hodot, B. B. Coal and Gas Outburst. Beijing, China, China Industry Press, 1966. (in Chinese)

Jiang, J., Yang, W., Cheng, Y., et al. Pore structure characterization of coal particles via MIP, N_2 and CO_2 adsorption: Effect of coalification on nanopores evolution. Powder Technology, 2019, 354: 136-148.

Ju, Y., Xi, C., Wang, S., et al. 3-D fracture evolution and water migration in fractured coal under variable stresses induced by fluidized mining: In situ triaxial loading and CT imaging analysis. Energy Reports, 2021, 7: 3060-3073.

Kenyon W. E. Petrophysical principles of applications of NMR Logging. The Log Analyst, 1997, 38: 21-43.

Kenyon, W. E., Day, P. I., Straley, C., et al. A three-part study of NMR longitudinal relaxation properties of water-saturated sandstones. SPE Formation Evaluation, 1988, 3(3): 622-636.

Leòn, C. New perspectives in mercury porosimetry. Advances in Colloid and Interface Science, 1998, 76-77: 341-372.

Li, Y., Song, D., Liu, S., et al. Evaluation of pore properties in coal through compressibility correction based on mercury intrusion porosimetry: A practical approach. Fuel, 2021, 291: 120130.

Li, Y., Lu, G., Rudolph, V. Compressibility and fractal dimension of fine coal particles in relation to pore structure characterisation using mercury porosimetry. Particle & Particle Systems Characterization, 1999, 16(1): 25-31.

Liu, W., Wang, G., Han, D., et al. Accurate characterization of coal pore and fissure structure based on CT 3D reconstruction and NMR. Journal of Natural Gas Science and Engineering, 2021, 96: 104242.

Liu, X., Zeng, Y., Wu, Q., et al. Ecological-based mining: A coal-water-thermal collaborative paradigm in ecologically fragile areas in western China. Engineering, 2024, 38: 209-222.

Liu, Z., Guo, P., Chen, R., et al. Online triaxial-NMR monitoring of pore-fracture reorganization and creep response in coal under a mining-type stress path. International Journal of Rock Mechanics and Mining Sciences, 2026, 201: 106462.

Lu, J., Jiang, W., Xie, H., et al. Dynamic disaster mechanism and acoustic emission evolution of deep coal-rock under true triaxial disturbance stress. Journal of Rock Mechanics and Geotechnical Engineering, 2025, 17(9): 5829-5844.

Manakov, A. Y., Shumskayte, M. Y., Mezin, A. A., et al. NMR transverse relaxation times and phase equilibria of methane hydrate in mesoporous alumina. Chemical Engineering Science, 2024, 299: 120436.

Mi, W., Wen, H., Fan, S., et al. Correlation analysis of injection parameters for low-medium pressure injection of liquid CO_2 for CH_4 displacement in coal seams. Energy, 2023, 278: 127760.

Ouyang, Z., Liu, D. M., Cai, Y., et al. Fractal analysis on heterogeneity of pore-fractures in middle-high rank coals with NMR. Energy & Fuels, 2016, 30(7): 5449-5458.

Pei, N., Zhao, J., Shi, X., et al. Evaluation of droplet evaporation characteristics and its influencing factors in high-temperature gaseous environment. Case Studies in Thermal Engineering, 2024, 56: 104274.

Shen, C., Cui, K., Wei, S., et al. Numerical simulation of water evaporation and migration characteristics of heat storage soil layer at pore scale. Applied Thermal Engineering, 2025, 277: 127090.

Tu, Q., Cheng, Y., Xue, S., et al. Energy-limiting factor for coal and gas outburst occurrence in intact coal seam. International Journal of Mining Science and Technology, 2021, 31(4): 729-742.

Wang, G., Han, D., Qin, X., et al. A comprehensive method for studying pore structure and seepage characteristics of coal mass based on 3D CT reconstruction and NMR. Fuel, 2020, 281: 118735.

Wang, G., Wang, E., Huang, Q., et al. Effects of cationic and anionic surfactants on long flame coal seam water injection. Fuel, 2022, 309: 122233.

Wang, H., Wang, H., Tan, J., et al. Recent progress of coal seam water injection technology for dust prevention: A comprehensive review. Advances in Geo-Energy Research, 2025, 16(3): 181-198.

Wei, Z., He, Z., Yang, J. Analysis of core temperature variation and its influencing factors in deep rock *in-situ* temperature-preserved coring. Advances in Geo-Energy Research, 2024, 14(3): 215-223.

Xie, H., Ju, Y., Gao, F., et al. Groundbreaking theoretical and technical conceptualization of fluidized mining of deep underground solid mineral resources. Tunnelling and Underground Space Technology, 2017, 67: 68-70.

Xie, H., Xie, J., Gao, M., et al. Theoretical and experimental validation of mining-enhanced permeability for simultaneous exploitation of coal and gas. Environmental Earth Sciences, 2015, 73(10): 5951-5962.

Xu, H., Zhai, C., Ranjith, P. G., et al. Pore-fracture evolution and fractal characteristics of coal under triaxial compression: Insights from *in-situ* nuclear magnetic resonance. International Journal of Rock Mechanics and Mining Sciences, 2026, 204: 106566.

Xu, L., Li, Y., Du, L., et al. Study on the effect of SDBS and SDS on deep coal seam water injection. Science of The Total Environment, 2023, 856: 158930.

Yang, M., Xu, J., Gao, J., et al. Study on water seepage law of confined coal body and optimization of water injection parameters. Fuel, 2023, 352: 129152.

Yao, Q., Chen, T., Tang, C., et al. Influence of moisture on crack propagation in coal and its failure modes. Engineering Geology, 2019, 258: 105156.

Yu, L., Yao, Q., Chong, Z., et al. Mechanical and microstructural damage mechanisms of coal samples treated with dry-wet cycles. Engineering Geology, 2022, 304: 106637.

Zhang, X., Zhang, X., Liu, J., et al. Multi-scale quantitative characterization of three-dimensional pores and fissures in deep coal and study of the evolution laws. Construction and Building Materials, 2024, 449: 138449.

Zheng, S., Yao, Y., Liu, D., et al. Nuclear magnetic resonance surface relaxivity of coals. International Journal of Coal Geology, 2019, 205: 1-13.

Zhou, H., Cao, Y., Xie, S., et al. Evolution of pore-fracture structure and mechanical properties of coal under dry-wet cycle. International Journal of Rock Mechanics and Mining Sciences, 2025, 192: 106146.

Zhu, X., Zaoui, A., Sekkal, W. Molecular-scale insight into improved waterproofing of cement paste by protective epoxy resins nano-coating. Powder Technology, 2023, 426: 118679.